Determination of strain fields and composition of self-organized quantum dots using x-ray diffraction

I. Kegel, T. H. Metzger, A. Lorke, and J. Peisl
CeNS at Sektion Physik, Ludwig-Maximilians-Universität München, D-80539 München, Germany

J. Stangl and G. Bauer
Institut für Halbleiterphysik, Johannes Kepler Universität, A-4040 Linz, Austria

K. Nordlund
Accelerator Laboratory, University of Helsinki, P.O. Box 43, FIN-00014 Helsinki, Finland

W. V. Schoenfeld and P. M. Petroff
Materials Department, University of California, Santa Barbara, California 93106
(Received 28 April 2000; published 2 January 2001)

We give a detailed account of an x-ray diffraction technique which allows us to determine shape, strain fields, and interdiffusion in semiconductor quantum dots grown in the Stranski–Krastanov mode. A scattering theory for grazing incidence diffraction is derived for the case of highly strained, uncapped nanostructures. It is shown that strain resolution can be achieved by ''decomposing'' the dots in their iso-strain areas. For a selected iso-strain area, it is explained how lateral extent, height above the substrate and radius of curvature can be determined from the intensity distribution around a surface Bragg reflection. The comparison of intensities from strong and weak reflections reveals the mean material composition for each strain state. The combination of all these strain resolved functional dependences yields tomographic images of the dots showing strain field and material composition.

DOI: 10.1103/PhysRevB.63.035318 PACS number(s): 68.65.−k, 61.10.−i

I. INTRODUCTION

A detailed understanding of the growth process of self-assembled semiconductor quantum dots[1–6] requires substantial knowledge about their internal structure. So far, external shape and lateral arrangement have been accessible by scanning microscopies.[7] Structural investigations with techniques like photoluminescence and Raman scattering are restricted to estimates of scalar physical quantities such as maxima or averages of strain or material composition. For a measurement of these quantities, which delivers spatial information, some kind of resolution is needed. The resolution can either be in real space, using a direct imaging approach as in transmission electron microscopy (TEM) or in reciprocal space as in an x-ray diffraction experiment[8] where spatial frequencies rather than spatial positions are probed.

The strengths of real space techniques lie in their broad applicability and the direct nature of their results. Relative drawbacks are the technologically demanding sample preparation and the limited statistics. In an x-ray diffraction experiment, the signal of a macroscopic portion of the sample's surface is integrated in the detector. A serious difficulty is the inaccessibility of the relative phase of the scattering process. Diffraction experiments thus usually require structural models with only a few variable parameters which are optimized to fit the measured data.[18,21] For example, the determination of the strain distribution within etched nanostructures using high resolution x-ray diffraction and grazing incidence diffraction is discussed in Refs. 9–17. Similarly, the lattice distortions in self-organized nanostructures have been determined in Refs. 18–22.

Apart from being a demanding task for a three-dimensional object of a few hundred thousand atoms with variable strain and material composition, these kinds of analyses are case studies, which are not highly generalizable. The kaleidoscopic wealth of different manifestations of self-assembled quantum dots calls for a more extensible and direct method for data evaluation.

In this paper, we present a detailed account of an analytical approach for the analysis of grazing incidence diffraction which allows us to extract tomographic images of strain fields and material composition in the dots. A different approach, which makes use of finite element calculations of the entire dot in order to simulate the scattering intensity[23] is less analytic but more synthetic. This method has the advantage of being applicable to *any* vertical and lateral concentration profile, but gives relatively little insight into the interdependence between real space structure and scattered intensity distribution. The approach presented here, on the other hand, provides a *physical understanding* of the relationship of strain-related phenomena in real and reciprocal space.

The paper is organized as follows: In Sec. II we discuss the concept of iso-strain scattering, in Sec. III the analytical formalism for the data evaluation is presented. After experimental considerations in Sec. IV we show results of a series of InAs/GaAs dots grown at different temperatures in Sec. V. The lateral composition profile and atomistic calculations of strain relaxation are discussed in Sec. VI.

II. DETERMINATION OF STRAIN AND SHAPE

A. Spatial distinction

In reciprocal space, the distance between two crystals is equivalent to the reciprocal difference of their lattice param-

 ©2001 The American Physical Society

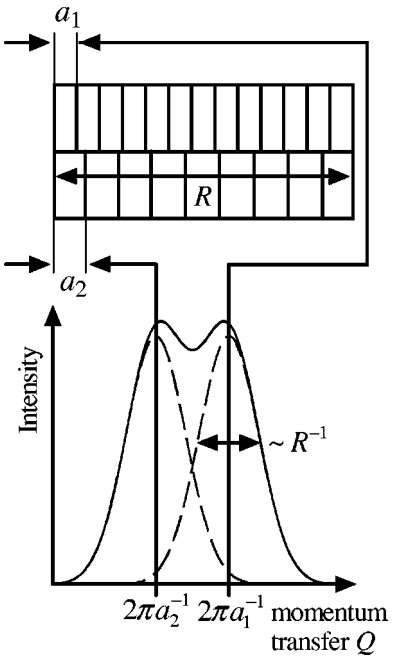

FIG. 1. Illustration of spatial distinction in hetero-epitaxial systems. Two regions may be distinguished if their difference in lattice parameter a_2-a_1 and size R are big enough to allow the resulting peaks in reciprocal space at $2\pi a_1^{-1}$ and $2\pi a_2^{-1}$ to be separated as two maxima.

eters. Therefore, two crystallites may be far apart in reciprocal space, even though they are spatially adjacent. For a lattice parameter difference of a few percent, the crystallites will yield two distinct peaks, whose half-widths can be used to analyze the size of each crystal (Fig. 1).

In this simple example there is an unspecific spatial *distinction*: two parts of a larger sample can be studied independently by tuning the scattering vector to the appropriate lattice parameters. As the lattice parameter difference between the two crystallites is reduced, the peaks merge until finally no distinction is possible anymore. This corresponds to the optical analogue of distinguishing two stars with a telescope. In this picture, the relative lattice parameter difference $\Delta a/a$ is equivalent to the smallest resolvable angle, a takes the place of the wavelength of light and the common size R of the crystallites corresponds to the telescope's aperture. For a mean lattice parameter a, the minimum percentual difference in lattice parameter is given by

$$\left(\frac{\Delta a}{a}\right)_{\min} = C\frac{a}{R}, \tag{1}$$

where C is a constant of the order of 1 which depends on the particular shape of the crystallites. Equation (1) clarifies the reciprocal relationship between spatial distinction and spatial extent of the regions of equal lattice parameter.

B. Iso-strain areas

If a nanocrystal has a lattice parameter which varies continuously from one end to the other, it may be thought of as being composed of a distribution of iso-strain areas.[20] For a particular Bragg reflection $\mathbf{Q}$, we define the iso-strain areas as the iso-surfaces of the appropriate scalar component ϵ of the strain field $\underline{\epsilon}$ which is determined as

$$\epsilon = \hat{\mathbf{Q}}^T \underline{\epsilon} \hat{\mathbf{Q}}, \tag{2}$$

where the hat on $\hat{\mathbf{Q}}$ denotes a unit vector. This definition compresses the full tensorial strain status of the nanocrystal into a scalar field by neglecting shear strains. The cumulative effect of these shear strains on the scattering process can be analyzed *after* the definition of the iso-strain area by calculating rotation matrices $\underline{\mathbf{R}}(\epsilon)$ whose rotation angles $\theta(\epsilon)$ and rotation axes $\mathbf{n}(\epsilon)$ are defined by

$$\cos\theta(\epsilon) = \frac{\hat{\mathbf{Q}}^T \cdot \int_{\mathrm{ISA}} \underline{\epsilon}\hat{\mathbf{Q}}\, da}{\left|\int_{\mathrm{ISA}} \underline{\epsilon}\hat{\mathbf{Q}}\, da\right|} = \frac{\epsilon}{|\langle \underline{\epsilon}\hat{\mathbf{Q}}\rangle_{\mathrm{ISA}}|},$$

$$\mathbf{n}(\epsilon) = \frac{\hat{\mathbf{Q}}\times\langle \underline{\epsilon}\hat{\mathbf{Q}}\rangle_{\mathrm{ISA}}}{|\langle \underline{\epsilon}\hat{\mathbf{Q}}\rangle_{\mathrm{ISA}}|}. \tag{3}$$

The average Bragg conditions $\mathbf{Q}_{\mathrm{ISA}}(\epsilon)$ are then located at

$$\mathbf{Q}_{\mathrm{ISA}}(\epsilon) = \frac{1}{1+\epsilon}\underline{\mathbf{R}}(\epsilon)\mathbf{Q} \approx (1-\epsilon)\underline{\mathbf{R}}(\epsilon)\mathbf{Q} \text{ for } \epsilon \ll 1. \tag{4}$$

Considering only scattering vectors in the plane $\mathcal{P}$ with normal $\mathbf{p}$ spanned by the incoming beam $\mathbf{k}_i$ and $\mathbf{Q}$, the projection of each iso-strain area onto $\mathcal{P}$ may be viewed as a two-dimensional crystal. From this point of view, each iso-strain area has a homogeneous, nondistorted lattice which scatters around the projected Bragg point.

For distortions which are anisotropic with respect to $\hat{\mathbf{Q}}$ and $\hat{\mathbf{Q}}\times\mathbf{p}$, the projected Bragg positions $\mathbf{Q}_{\mathrm{ISA}}^{\mathrm{proj}}(\epsilon)$ are given by

$$\mathbf{Q}_{\mathrm{ISA}}^{\mathrm{proj}}(\epsilon) \approx (1-\epsilon)[\underline{\mathbf{R}}(\epsilon)\mathbf{Q} - \mathbf{p}(\underline{\mathbf{R}}(\epsilon)\mathbf{Q}\cdot\mathbf{p})], \tag{5}$$

defining a new matrix $\underline{\mathbf{R}}^{\mathrm{proj}}(\epsilon)$ such that

$$\mathbf{Q}_{\mathrm{ISA}}^{\mathrm{proj}}(\epsilon) \approx (1-\epsilon)\underline{\mathbf{R}}^{\mathrm{proj}}(\epsilon)\mathbf{Q} \quad \text{for } \epsilon \ll 1. \tag{6}$$

For isotropic distortions with respect to $\hat{\mathbf{Q}}$ and $\hat{\mathbf{Q}}\times\mathbf{p}$, the shear components in the plane $\mathcal{P}$ will average out giving $\mathbf{n}(\epsilon) = \hat{\mathbf{Q}}\times\mathbf{p}$. In this case, $\underline{\mathbf{R}}^{\mathrm{proj}}(\epsilon) = \underline{\mathbf{1}}$ in Eq. (6) and the projected Bragg points of the iso-strain areas are associated with momentum transfers which are scalar multiples of $\mathbf{Q}$.

C. Spatial resolution

Spatial *resolution* implies the determination of the relative position of the two crystallites. While there is no generic procedure to determine relative arrangements for the general case, self-assembled quantum dots grown in the Stranski–Krastanov (SK) mode are subject to boundary conditions which reduce the three-dimensional positional difference to a one-dimensional scalar value. In SK systems, the stress energy that builds up during the growth of mismatched hetero-

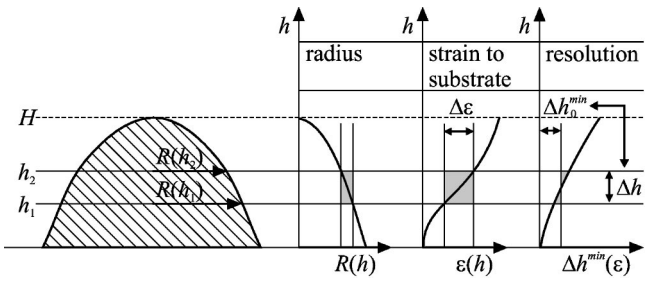

FIG. 2. Schematic functional dependence of strain, height, and resolution in islands grown in the SK mode. Radius R and strain to substrate ϵ are required to calculate the local minimum height difference $\Delta h^{\min}$ to resolve two parts of the nanostructure. In the particular case shown in the figure, the heights h_1 and h_2 are resolvable since their height difference Δh exceeds the mean local minimum value of $\Delta h_0^{\min}$.

epitaxial layers is lowered through the formation of three-dimensional nanometer-sized islands, whose crystalline structure remains coherent to the underlying substrate. This coherency demands that the lattice parameter parallel to the surface normal is relaxed from bottom to top, leading to the decomposition into iso-strain areas as explained in Sec. II B.

Changing the selected strain state by adjusting the total momentum transfer $\mathbf{Q}$ to a different $\mathbf{Q}_{\mathrm{ISA}}^{\mathrm{proj}}(\epsilon)$ thus corresponds to a change in *height* above the sample's surface (Fig. 2). Assuming the height above the surface $h(\epsilon)$ to be a monotonic function of the strain state ϵ and rewriting Eq. (1) in reciprocal space coordinates as

$$\Delta\epsilon \approx C\frac{2\pi}{R(\epsilon)Q} \quad \text{for} \quad \epsilon \ll 1 \tag{7}$$

gives an expression for the minimum resolvable height difference in the crystallite:

$$\Delta h^{\min}(\epsilon) \approx h'(\epsilon)\Delta\epsilon = Ch'(\epsilon)\frac{2\pi}{R(\epsilon)Q}. \tag{8}$$

The above resolution element has two important features: first, the proportionality to $h'(\epsilon)$ is equivalent to an inverse proportionality to the strain gradient $\epsilon'(h)$, i.e., the faster the lattice parameter changes with height, the better is the resolution. Regarding the material properties of hetero-epitaxial systems, this corresponds to better resolutions for higher lattice mismatches. Second, the resolution element is inversely proportional to the lateral size of the iso-strain areas. In summary, spatial resolution can be achieved for large enough nanocrystals with high enough lattice mismatch with respect to the substrate such that

$$\Delta h(\epsilon) < H, \tag{9}$$

where H is the total height of the nanocrystal.

D. Iso-strain scattering

Let us suppose the projections of the iso-strain areas on $\mathcal{P}$ have shape functions $f_{x_z}(x_r, x_a)$ where x_r is the coordinate of the radial axis along $\mathbf{Q}$ and x_a is measured along the angular direction perpendicular to it. The resulting third axis parallel to $\mathbf{p}$ is written as x_z. Without restricting the general validity, we assume these projections to be rectangular meshes with the primitive lattice vectors along x_r and x_a. In this section, we only consider momentum transfers with zero components normal to $\mathcal{P}$ $(q_z = 0)$ for which the three-dimensional shape of the iso-strain areas is irrelevant. For the reciprocal coordinates q_r and q_a relative to the Bragg-point $\mathbf{Q}$ of the substrate, the phase sum of all lattice points integrated over all iso-strain areas stacked along $\mathbf{p}$ is

$$F(q_r, q_a) = \int dx_z \sum_{\substack{(n_r, n_a) \\ \in \Omega(x_z)}} e^{i(Q+q_r)x_{n_r}(x_z)} e^{iq_a x_{n_a}(x_z)}$$

with

$$x_{n_{r,a}}(x_z) = (n_{r,a} + \delta_{r,a}(x_z))a_{r,a}(x_z),$$

$$\Omega(x_z) = \{(n_r, n_a) \in \mathbb{N}^2 \,|\, f_{x_z}(x_{n_r}(x_z), x_{n_a}(x_z)) > 0\}, \tag{10}$$

where $a_{r,a}(x_z)$ is the real space lattice parameter parallel to $x_{r,a}$ and $\delta_{r,a}(x_z)$ designates the required shift to adjust the origin of the lattice at a specified x_z (see Fig. 3). Since only the values of x_r are relevant for the following argument, this simple model even holds for the case of varying anisotropies. For calculations in reciprocal space, an effective reciprocal lattice parameter $g_{\mathbf{Q}} = 2\pi a_r^{-1}\sqrt{h^2+k^2+l^2}$ is used, where h, k, and l are the indices pertaining to the reflection $\mathbf{Q}$.

Here, a subtle problem arises when trying to rewrite this phase sum in continuous coordinates: the origin of the coordinate system in real space must be chosen and fixed for the whole calculation while discrete lattice points are still used. The reason for this stems from the fact that the value of x_z in Eq. (10) not only influences the position of the Bragg condition along q_r for the corresponding iso-strain area, but also introduces a phase shift which depends on the alignment of lattice points in subsequent lattice planes. This information will be lost when neglecting the quantization of the lattice and has to be added to the integrals as a phase function $\phi(x_z)$ which is dependent on the origin of the discrete coordinates. Although $\phi(x_z)$ is determined by $\delta_r(x_z)$ alone, the determination of both $\delta_r(x_z)$ and $\delta_a(x_z)$ allows us to extend our result to all reflections parallel to $\mathcal{P}$ without going back to Eq. (10).

If there exists a line of coherence parallel to $\mathbf{p}$ along which the lattice points of different x_z are stacked with zero shifts, the origin for x_r and x_a is most conveniently chosen on this line, as $\delta_{r,a}(x_z)$ will then vanish for all values of x_z and $\phi(x_z)$ will be unity throughout the whole crystal. For the case of nanostructures which are axially symmetric with respect to $\mathbf{p}$, a symmetry argument shows that the line of coherence must coincide with the line of symmetry.

The sum in Eq. (10) may thus be approximated by a convolution of the form factor $\tilde{F}_{x_z}(q_r, q_a)$ of the iso-strain area at x_z with a delta function around the appropriate Bragg peak at $g_{\mathbf{Q}}(x_z) - Q$ along q_r multiplied by the phase factor $\phi(x_z)$:

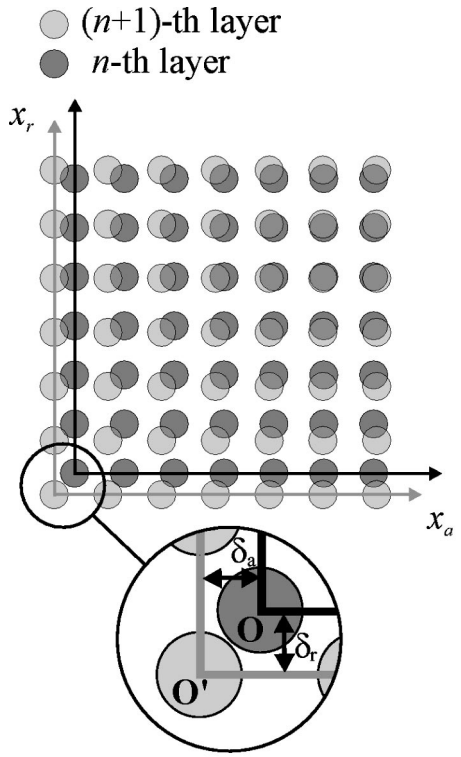

FIG. 3. Determination of offsets in lattice origins for the discrete phase sum of two different iso-strain areas. For two subsequent layers n and $n+1$ with different lattice parameters, the origins of the lattices **O** and **O**′ are subject to positional shifts δ_a and δ_r in the angular and radial directions x_a and x_r. The functional dependence of the radial shift δ_r strongly influences the intensity distribution in reciprocal space.

$$F(q_r,q_a)=\int dx_z \int \tilde{F}_{x_z}(u,q_a)\phi(x_z) \times \delta(u-q_r+(g_{\mathbf{Q}}(x_z)-Q))du$$

with

$$\tilde{F}_{x_z}(q_r,q_a)=\int\int f_{x_z}(x_r,x_a)e^{iq_r x_r+iq_a x_a}\,dx_r\,dx_a. \quad (11)$$

In order to simplify Eq. (11), it has to be noted that for a selected reciprocal coordinate q_r^0 the integral over x_z will have relevant contributions only in a certain range Δx_z around the position x_z^0 where the Bragg condition is fulfilled. Taking Eq. (7) into account and assuming $g_{\mathbf{Q}}(x_z)$ to be a monotonic function, the upper and lower limits for Δx_z are given by

$$x_z^{\pm}=g_{\mathbf{Q}}^{-1}\left(g_{\mathbf{Q}}(x_z^0)\pm C\frac{2\pi}{R(x_z^0)}\right) \approx x_z^0 \pm C\frac{2\pi\ dg_{\mathbf{Q}}^{-1}}{R(x_z^0)\ dq_r}\bigg|_{q_r=g_{\mathbf{Q}}(x_z^0)} \quad (12)$$

which gives an estimate for Δx_z:

$$\Delta x_z \approx C\frac{2\pi}{R(x_z^0)}\left(\frac{dg_{\mathbf{Q}}}{dx_z}\right)^{-1}\bigg|_{x_z=x_z^0}. \quad (13)$$

If spatial resolution can be achieved as explained in Sec. II C, the range given by Δx_z will be a subset of the entire range of the integration given by the size of the nanostructure.

Two approximations can now be made with respect to the relevant range of integration:

First, the shape function of the projected iso-strain area can be considered constant in Δx_z which is strictly valid for

$$\Delta x_z \frac{1}{R(x_z^0)}\frac{dR}{dx_z}\bigg|_{x_z=x_z^0} \ll 1. \quad (14)$$

In that case, the index x_z on $\tilde{F}$ in Eq. (11) should be renamed to x_z^0.

Second, the reciprocal lattice parameter can be approximated as a linear function throughout Δx_z:

$$g_{\mathbf{Q}}(x_z)=g_{\mathbf{Q}}(x_z^0)+g'_{\mathbf{Q}}(x_z^0)(x_z-x_z^0). \quad (15)$$

In addition, we can further simplify the expression by restricting the analysis to structures which have a line of vertical coherence by choosing the origin for x_r and x_a at the line of symmetry. As discussed above, we can then set $\phi(x_z)=1$. The scattering amplitude for these approximations is obtained as

$$F(q_r^0,q_a)=\int \tilde{F}_{x_z^0}(q_r-g_{\mathbf{Q}}(x_z^0)+Q+g'_{\mathbf{Q}}(x_z^0)x_z,q_a)dx_z. \quad (16)$$

If the relevant range of integration Δx_z lies wholly within the nanostructure, the bounds of the x_z integration in Eq. (16) may be extended to infinity whereby the constant offset in the first argument becomes arbitrary and can be omitted. The resulting simplified expression is written as

$$F(q_r^0,q_a)=(g'_{\mathbf{Q}}(x_z^0))^{-1}\int \tilde{F}_{x_z^0}(u,q_a)du. \quad (17)$$

Rewriting the integral in Eq. (17) in terms of the real-space shape function $f_{x_z^0}$ leads to

$$F(q_r^0,q_a)=(g'_{\mathbf{Q}}(x_z^0))^{-1}\int f_{x_z^0}(0,x_a)e^{iq_a x_a}\,dx_a. \quad (18)$$

In summary, the angular scattering amplitude is given by the *one-dimensional* Fourier transform of the linear section through the shape function perpendicular to **Q** and **p**. If the sections are single contiguous intervals of length $D_{\mathbf{Q}}(x_z^0)$, the remaining integral can be calculated as

$$F(q_r^0,q_a)=(g'_{\mathbf{Q}}(x_z^0))^{-1}\frac{\sin\frac{1}{2}q_a D_{\mathbf{Q}}(x_z^0)}{\frac{1}{2}q_a}. \quad (19)$$

The scattering intensity is thus proportional to the inverse square of the reciprocal lattice parameter gradient and falls off as q^{-2} along q_a. In summary, the lateral form factor of iso-strain scattering along q_a is determined exclusively by

the section length of the two-dimensional *projection* of the iso-strain area along x_a and is independent of the actual shape of the projection.

III. HEIGHT RESOLUTION FOR NANOCRYSTALS ABOVE A SURFACE

A. Four-process scattering

In scattering geometries of grazing incidence or exit where the angles of incidence (α_i) and exit (α_f) are comparable to the critical angle of total external reflection (α_c), the Born approximation is no longer accurate and refraction effects have to be taken into account.[24] For a plain surface, the structure factor of the sample is modulated by the product of the transmission functions

$$t_{i,f}(\alpha_{i,f}) = \frac{2\sin\alpha_{i,f}}{\sin\alpha_{i,f} + \sqrt{\sin^2\alpha_{i,f} - \sin^2\alpha_c}} \tag{20}$$

describing the changes in field strength as the beam enters and exits the sample through the surface. For strained nanostructures on top of the surface, the optical part of the scattering process additionally includes multiple scattering between the surface and the nanostructures above it.

Since strain-driven island formation in the Stranski–Krastanov growth mode leads to nanostructures which are coherent at the substrate interface but with continuously relaxing lattice parameter towards the top, the lattice parameter values in the island are nowhere present in the substrate, apart from very small distortions. By selecting a total momentum transfer which corresponds to a certain lattice parameter in the island, one excludes Bragg scattering contributions from the substrate. In first order perturbation theory, the surface acts like a mirror, doubling the incoming and the diffracted beam as shown in Fig. 4.

In the following calculations involving surface reflections we fix the reciprocal coordinates q_r at an arbitrary q_r^0 and q_a at 0 and consider the dependence of the structure factor on the angles of incidence (α_i) and exit (α_f) which was set aside in Sec. II. Each scattering process has a different vertical momentum transfer q_z dependent on the angles of incidence and exit for the Bragg scattering process. Furthermore, each resulting structure factor $F^z(q_z)$ has a different relative amplitude which is given by the product of all reflectivities r involved in the particular scattering sequence. The total scattering amplitude $F_{\text{total}}(\alpha_i,\alpha_f)$ then results as

$$F^z_{\text{total}}(\alpha_i,\alpha_f) = F^z(q_{z,1}) + r(\alpha_i)r(\alpha_f)F^z(q_{z,2}) + r(\alpha_i)F^z(q_{z,3}) + r(\alpha_f)F^z(q_{z,4})$$

with

$$\begin{aligned} q_{z,1} &= k(\alpha_i + \alpha_f),\\ q_{z,2} &= k(-\alpha_i - \alpha_f),\\ q_{z,3} &= k(-\alpha_i + \alpha_f),\\ q_{z,4} &= k(\alpha_i - \alpha_f), \end{aligned} \tag{21}$$

where k is the length of the wave vector of the incoming beam.

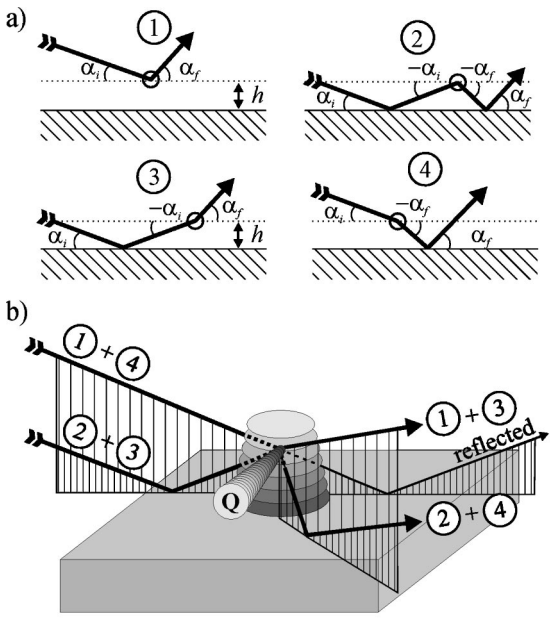

FIG. 4. Four scattering processes from first order perturbation theory. Part (a) shows a side view of the four processes which interfere coherently and give rise to a generalized optical function for grazing incidence diffraction. The process labeled as (1) is the direct Bragg reflection at the iso-strain area selected by the total momentum transfer **Q**. Process (2) employs two ordinary reflections from the surface before and after Bragg reflections at grazing angles of α_i and α_f, respectively. The actual Bragg scattering is denoted by a circle. Process (3) and (4) each involve one of those substrate reflections. The three-dimensional beam paths are shown in part (b). The total momentum transfer **Q** which is parallel to the surface requires the diffracted beams to be deflected out of the plane of incidence.

B. Vertical structure factor in iso-strain scattering

Equation (21) is valid for arbitrary nanostructures above a plain surface. Including the phase factor $e^{iq_z x_z}$ for a finite q_z in Eq. (16) leads to an expression which is more general than Eq. (17):

$$F(q_r^0,q_a,q_z) = (g'_{\mathbf{Q}}(x_z^0))^{-1} e^{iq_z x_z^0} \times \int \tilde{F}_{x_z^0}(u,q_a) e^{iq_z (g'_{\mathbf{Q}}(x_z^0))^{-1} u}\, du. \tag{22}$$

Now, the curvature of the iso-strain areas is neglected. This is a valid approximation if the mean height is larger than the vertical extension of the iso-strain area. By writing out the Fourier transforms Eq. (22) becomes

$$F(q_r^0,q_a,q_z) = (g'_{\mathbf{Q}}(x_z^0))^{-1} e^{iq_z x_z^0} \times \int f_{x_z^0}\left(\frac{q_z}{g'_{\mathbf{Q}}(x_z^0)}, x_a\right) e^{iq_a x_a}\, dx_a. \tag{23}$$

Generalizing the notion of sections as in Eq. (19) to $D_{\mathbf{Q}}(x_z^0,x_a)$ so as to include an arbitrary angular distance

from the line of vertical coherence, gives an expression for the structure factor for nonzero q_z:

$$F(q_r^0,q_a,q_z)=(g'_{\mathbf{Q}}(x_z^0))^{-1}e^{iq_zx_z^0}\times\frac{\sin\frac{1}{2}q_aD_{\mathbf{Q}}(x_z^0,q_z(g'_{\mathbf{Q}}(x_z^0))^{-1})}{\frac{1}{2}q_a}. \quad (24)$$

The q_z dependence of the structure factor at $q_a=0$ is thus determined by the weighted projection of the shape function onto x_a:

$$F^z(q_z)=F(q_r^0,0,q_z)=(g'_{\mathbf{Q}}(x_z^0))^{-1}e^{iq_zx_z^0}D_{\mathbf{Q}}\left(x_z^0,\frac{q_z}{g'_{\mathbf{Q}}(x_z^0)}\right). \quad (25)$$

Equation (25) shows that $F^z(q_z)$ will be zero above a maximum value $q_z^{0,\max}$ which is given by the maximum lateral extent $x_a^{0,\max}$ and the reciprocal lattice parameter gradient at x_z^0:

$$q_z^{0,\max}=x_a^{0,\max}g'_{\mathbf{Q}}(x_z^0). \quad (26)$$

Close to the lower and upper limit in x_z of the nanostructure where the iso-strain approximations fail, $F(q_z)$ will be smoothed out, especially near $q_z^{0,\max}$ above which it will still give nonzero values.

C. Generalized optical functions

Now we restrict the calculation to cases where the iso-strain areas are sufficiently large and the weighted projection of the shape function along x_a is varying slowly enough at small q_z to neglect the shape dependence of $F(q_z)$ at angles of incidence and exit which are comparable to α_c. For cross sections with smooth outlines near $x_r=0$ this leads to

$$F^z(q_z)\approx e^{iq_zx_z^0} \quad \text{for} \quad q_z\simeq k\alpha_c \quad (27)$$

and is strictly correct when

$$\frac{1}{F^z(0)}\frac{dF^z(q_z)}{dq_z}\bigg|_{q_z=0}k\alpha_c=\frac{1}{D_{\mathbf{Q}}(x_z^0,0)}\frac{dD_{\mathbf{Q}}(x_z^0,q_z)}{dq_z}\bigg|_{q_z=0}k\alpha_c \ll 1 \quad (28)$$

is fulfilled. If either the angle of incidence (α_i) or the angle of exit (α_f) is larger than α_c, the term with q_z^0 becomes dominant as the other three terms scale with the reflectivity of the substrate.

Inserting this approximation into Eq. (21) and factorizing out $e^{ik(\alpha_i+\alpha_f)x_z^0}$ the total amplitude is obtained as

$$F^z_{\text{total}}(\alpha_i,\alpha_f)=F^z(k(\alpha_i+\alpha_f))e^{ik(\alpha_i+\alpha_f)}\times(1+r(\alpha_i)r(\alpha_f)e^{-2ik(\alpha_i+\alpha_f)x_z^0}+r(\alpha_i)e^{-2ik\alpha_ix_z^0}+r(\alpha_f)e^{2ik\alpha_fx_z^0}). \quad (29)$$

By factorizing the parentheses in Eq. (29) one can now separate the dependencies on α_i and α_f which are found to be identical. This relationship can thus be expressed as

$$F^z_{\text{total}}(\alpha_i,\alpha_f)=F^z(k(\alpha_i+\alpha_f))t^{\text{fps}}(\alpha_i,x_z^0)t^{\text{fps}}(\alpha_f,x_z^0)$$

with

$$t^{\text{fps}}(\alpha,z)=1+r(\alpha)e^{-2ik\alpha z}. \quad (30)$$

The functional form of the total amplitude F^z_{total} is now analogous to the case of a flat surface with F^z derived in Sec. III B assuming the role of the structure factor and t^{fps} as a generalized optical function in place of the transmission function, with t^{fps} including the effects of the four-process scattering (fps). Indeed, for $z=0$ one finds that

$$t^{\text{fps}}(\alpha,0)=1+r(\alpha)=t(\alpha) \quad (31)$$

is the same function as in Eq. (20).

For a discussion of the scattered intensity we analyze the absolute square of t^{fps},

$$I^{\text{fps}}(\alpha,z)=|t^{\text{fps}}(\alpha,z)|^2=(1+r(\alpha)e^{-2i\alpha z})(1+r^*(\alpha)e^{2ik\alpha z})=1+|r(\alpha)|^2+2\Re(r(\alpha))\cos 2k\alpha z+2\Im(r(\alpha))\sin 2k\alpha z. \quad (32)$$

At this point it is convenient to continue with the reduced coordinates

$$\hat{\alpha}=\frac{\alpha}{\alpha_c},\quad \hat{z}=k\alpha_cz. \quad (33)$$

Since α is of the order of α_c, which is typically a few mrad, the reflectivity and the transmittivity are usually written as

$$r(\hat{\alpha})=\frac{\hat{\alpha}-\sqrt{\hat{\alpha}^2-1}}{\hat{\alpha}+\sqrt{\hat{\alpha}^2-1}},\qquad t(\hat{\alpha})=\frac{2\hat{\alpha}}{\hat{\alpha}+\sqrt{\hat{\alpha}^2-1}}, \quad (34)$$

not taking roughness effects into account. Due to the square root in Eq. (34) there are two regimes for $\hat{\alpha}<1$ and $\hat{\alpha}>1$ which have to be dealt with separately.

For $\hat{\alpha}<1$ in Eq. (34), it is convenient to separate real and imaginary parts by taking $(-i)$ out of the square roots in r:

$$r(\hat{\alpha})=(2\hat{\alpha}^2-1)+i(2\hat{\alpha}\sqrt{1-\hat{\alpha}^2}). \quad (35)$$

Evidently, $|r(\hat{\alpha})|^2=1$ and therefore

$$I^{\text{fps}}(\hat{\alpha},\hat{z})=2+2(2\hat{\alpha}^2-1)\cos 2\hat{\alpha}\hat{z}+4\hat{\alpha}\sqrt{1-\hat{\alpha}^2}\sin 2\hat{\alpha}\hat{z}. \quad (36)$$

The angle of maximum intensity $\hat{\alpha}^{\max,1}$ in Eq. (36) is implicitly given by

$$\hat{\alpha}^{\max,1}=\cos\hat{\alpha}^{\max,1}\hat{z}. \quad (37)$$

For the case of an iso-strain area where the Bragg scattering only occurs at a certain height above the sample's surface, one can measure the maximum and determine the height z from

$$z=\frac{1}{k\alpha^{\max,1}}\arccos\frac{\alpha^{\max,1}}{\alpha_c}. \tag{38}$$

Beyond the critical angle ($\hat{\alpha}>1$), the generalized optical function is a harmonic oscillation of period $2\hat{z}$ whose amplitude decays as $\hat{\alpha}^{-1}$ on top of a background which asymptotically decays towards unity as $\hat{\alpha}^{-2}$:

$$I^{\mathrm{fps}}(\hat{\alpha},\hat{z})=1+\frac{2\hat{\alpha}^2-1-2\hat{\alpha}\sqrt{\hat{\alpha}^2-1}}{2\hat{\alpha}^2-1+2\hat{\alpha}\sqrt{\hat{\alpha}^2-1}}+2\frac{\hat{\alpha}-\sqrt{\hat{\alpha}^2-1}}{\hat{\alpha}-\sqrt{\hat{\alpha}^2-1}}\cos 2\hat{z}\hat{\alpha}. \tag{39}$$

The position of the first maximum of the oscillatory part $\alpha^{\max,2}$ thus also gives the height z of the iso-strain area,

$$z=\frac{\pi}{k\alpha^{\max,2}}. \tag{40}$$

Figure 5 shows how the maximum of the classic transmission function ($\hat{z}=0$) at $\hat{\alpha}=1$ shifts to lower $\hat{\alpha}$ for larger $\hat{z}$. As the sharp transmission peak is smoothed and broadened, a minimum starts to form at $\hat{\alpha}>1$ moving towards lower angles together with the first pronounced maximum. In fact, at $\hat{\alpha}=1$, where a strong maximum is expected for traditional grazing incidence diffraction, the absolute square of the generalized optical function

$$I^{\mathrm{fps}}(1,\hat{z})=2(1+\cos 2\hat{z}) \tag{41}$$

falls to zero for $\hat{z}=\pi/2$.

IV. EXPERIMENTAL CONSIDERATIONS

In order to combine the analytical techniques described in Secs. II and III, a grazing incidence and exit geometry[25] is most appropriate (Fig. 6). In this case, the total momentum transfer lies predominantly in the plane of the sample's surface. The direction **p** which can be thought of as the stacking direction for the projected iso-strain areas is then parallel to the surface normal, i.e., the direction in which stress in heteroepitaxial systems can be relieved by means of strain. For centro-symmetrical islands, this configuration has the added advantage that the line of symmetry is also parallel to **p** and can be taken as the origin for the lateral coordinates x_r and x_a. Furthermore, for angles of incidence and exit below the critical angle of total external reflection, the penetration depth of the evanescent x-ray beam below the surface is of the order of 5–10 nm,[26] maximizing the relative scattering power of the dots with respect to the substrate.

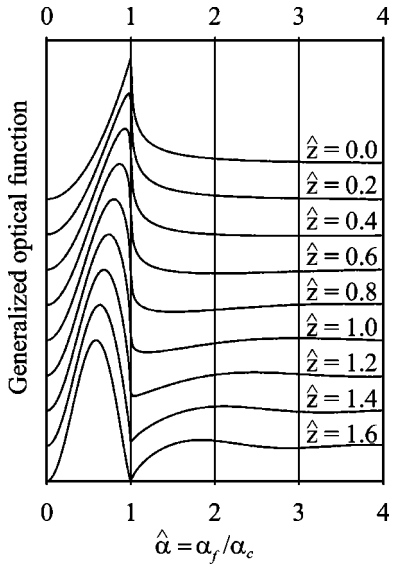

FIG. 5. Generalized optical functions for various reduced heights $\hat{z}$. The sharp maximum at $\hat{z}=0$ is seen to move to smaller angles $\hat{\alpha}$ for increasing $\hat{z}$, at the same time assuming a broader and symmetric shape. Near $\hat{z}=\pi/2$ the intensity is modulated to zero. The oscillatory behavior in the range $\hat{\alpha}>1$ which becomes apparent for $\hat{z}>1$ is due to the intuitive mirror effect of an iso-strain area above a reflecting surface.

The applicability of the presented analytical methods is limited by the size and strain gradient of the islands and their functional dependencies on the height above the surface. If the lateral size R becomes too small, the fundamental requirement of spatial distinction described in Sec. II A breaks down. Likewise, if the strain gradient g' is too small, the insufficient spreading in reciprocal space will prohibit the differentiation of spatial regions. For a given height H of the island, these prerequisites can be commonly expressed as a rule of thumb:

$$\eta=Rg'H\gg 1. \tag{42}$$

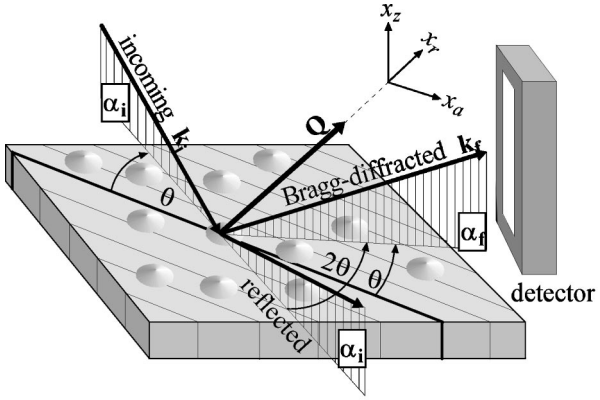

FIG. 6. Scattering geometry for grazing incidence and exit. Both the angle of incidence α_i and the angle of exit α_f are close to the critical angle of total external reflection α_c. Diffraction takes place on lattice planes which are perpendicular to the sample's surface. The intensity is measured by a position sensitive detector which records α_f spectra.

The dimensionless system constant η thus quantifies the goodness of the iso-strain approximation. For a typical system of lateral size 50 nm, exhibiting a lattice parameter difference of 5% along a height of 10 nm and a measurement at a total momentum transfer of 4 Å^{-1}, η has a numerical value of 100.

For too small R, the system enters the size regime of atomic defects which has its own methods for the analytical treatment of the scattering intensity.[27] For too small g' at large R, the strain effects are best treated as corrections to the strainless case. While the values of R and H are fixed for a particular system, the numerical value of g' can be increased by choosing a higher order reflection.

The determination of heights with Eq. (38) has different accuracies for small and large values of $\hat{z}$. While the deviation of the first pronounced maximum is substantial for values of $\hat{z}>0.2$, for values smaller than that, a highly accurate knowledge of the critical angle α_c and a good resolution in α_f is required. Equation (40) on the other hand, shows a reciprocal behavior to Eq. (38) where the accuracy is high for small $\hat{z}$ and low for large $\hat{z}$. However, the rapidly decaying amplitude of the oscillatory part in Eq. (39) and the decaying structure factor derived in Sec. III B are unfavorable for the experimental determination of this maximum.

Realistic iso-strain areas will not be flat but curved. Although this fact does not constitute a problem for the iso-strain scattering formalism presented in Sec. II D, the determination of height in Sec. III C is based on a single height z above the surface. If the vertical extent introduced by the curvature is small compared to the height z of the iso-strain area under consideration, it can be neglected. However, also for substantial curvatures, the shift of the first pronounced maximum of the generalized optical function in Eq. (32) describes a mean weighted height of the iso-strain area.

All calculations in Secs. II and III neglect the variation of lateral size R and strain gradient g' within the relevant range of integration Δx_z as defined in Eq. (13). In general, these assumptions may not be very well fulfilled, with values for η up to 0.5 still describing realistic situations. These deviations from the idealizations leading to Eqs. (19) and (38) result in an averaging over the parameters R and g'. Thus, even while the scatterered intensity may not be closely traced by the theoretical curves, the main features will stand out and mean values of R, g', and z can be obtained.

V. RESULTS AND DISCUSSION

Samples were grown by molecular beam epitaxy (MBE) on semi-insulating GaAs (001) substrates. First a 200 nm GaAs buffer layer and AlAs/GaAs (2 nm/10 nm) short period superlattice were grown to obtain a smooth growth surface. This was followed by a 150 nm GaAs layer grown at 600 °C. The sample temperature was then reduced to the InAs island growth temperature (450 °C to 530 °C) as determined using a pyrometer. Once at growth temperature, the InAs islands were formed using alternating beam epitaxy (ABE). Island formation was monitored by reflection high energy electron diffraction (RHEED). Immediately after formation of the InAs islands the substrate temperature was reduced. As shown by atomic force microscopy, the chosen growth conditions lead to rotationally symmetric quantum dots, with a random lateral arrangement of dot positions. Dislocations are not expected for this range of growth parameters.

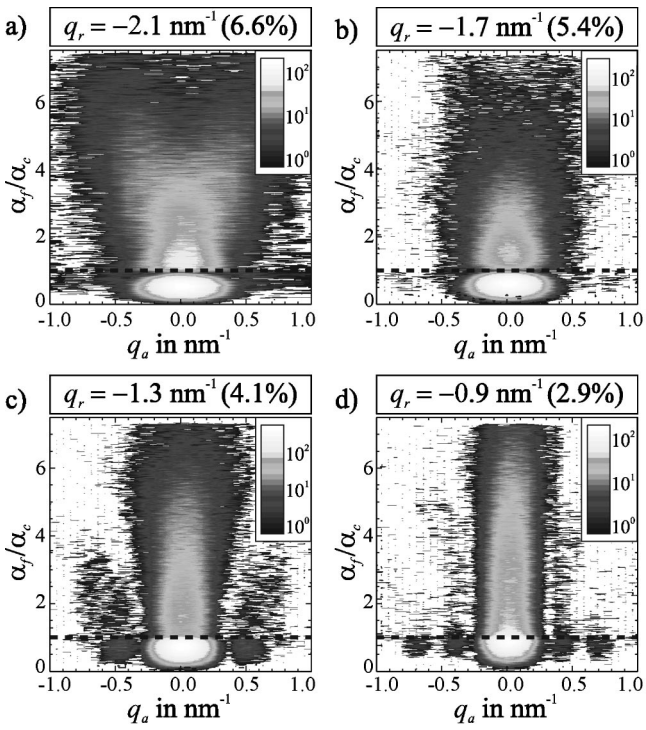

FIG. 7. Four exemplary two-dimensional reciprocal space maps in the (q_a, α_f) plane. The collection of 16 such maps constitute the three-dimensional map of reciprocal space between the two reflections of GaAs and InAs. The four maps display increasing values of q_r which corresponds to a decreasing lattice parameter difference between the selected iso-strain area and the substrate. The difference in percent is given in parentheses after the value of q_r. Clearly visible features are the narrowing of the central maximum at $\alpha_f < \alpha_c$ with decreasing lattice parameter difference corresponding to an increase in the lateral size of the dot towards the substrate and the increase of the α_f position of the global maximum which indicates lower heights for decreasing strain.

All measurements have been performed at the TROÏKA II beamline at the European Synchrotron Radiation Facility (ESRF) in Grenoble at a wavelength of 1.5 Å. Here, we show results measured between the (220) reflections of GaAs and InAs, where three-dimensional mappings of reciprocal space are performed. To this end, a position sensitive detector (see Fig. 7) records α_f spectra in angular scans along q_a which are repeated at successive radial positions q_r. Each value of q_r corresponds to a different strain state. Given that the iso-strain approximations presented in Sec. II are valid (see Sec. IV), only the close vicinity of the selected iso-strain area contributes to the scattering intensity at this point. The scattering from this tiny portion of the near-surface parts of the sample is detectable due to the diffraction condition which effectively blinds out all other strain states. The electromagnetic field was additionally constrained to the

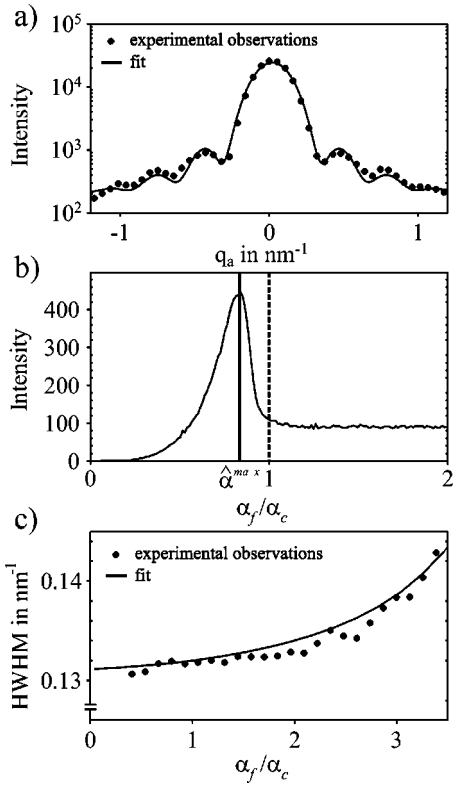

FIG. 8. Three-step analysis of the reciprocal space map shown in Fig. 7(d). Part (a) shows the determination of lateral size using the $\sin x/x$ law of Eq. (19). Allowing for a size distribution of a few percent, the functional dependence is well followed. The height of the iso-strain area is determined in (b). The position of the optical maximum at $\hat{\alpha}^{\max}$ differs from 1 as would be expected for grazing incidence diffraction on planar surfaces. The actual height is then calculated from Eq. (38). The curvature fit is displayed in (c). Here, the half-widths of the central maximum for different values of α_f are fitted with a hollow sphere of variable radius of curvature.

near-surface region by choosing an incident angle of 0.2°, well below the critical angle of total external reflection at 0.28°.

Each angular scan of a three-dimensional mapping results in a two-dimensional reciprocal space map (RSM). The analysis of the scattering intensity proceeds by evaluating three different aspects of the RSMs for each radial position q_r. First, the angular variation of the scattering intensity integrated for α_f up to α_c [Fig. 8(a)] is fitted using Eq. (19) yielding the lateral size of the iso-strain area. In the present case of axially symmetric islands, this corresponds to the radius of the circular projection of the iso-strain area. Second, the mean height of the iso-strain area above the surface is determined from the position of the first pronounced maximum of the scattering intensity along α_f [Fig. 8(b)]. To improve statistics, for each value of α_f the RSM is integrated along q_a in the range of the central maximum. The numerical value of the height z is calculated using Eq. (38). In order to obtain an estimate for the curvature of the iso-strain areas, the half-width of the central maximum along q_a is plotted as a function of α_f [Fig. 8(c)]. The variation in curvature due to the lateral shape as given by Eq. (24) typically accounts to

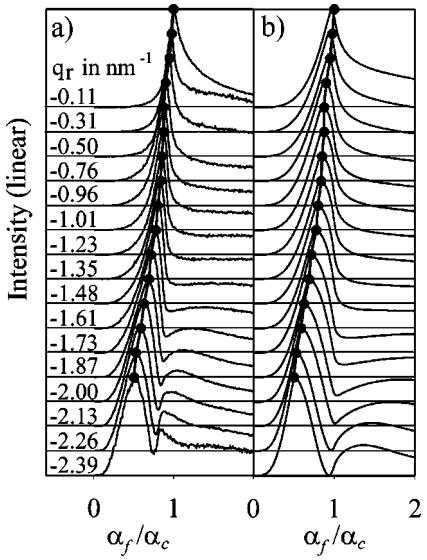

FIG. 9. Comparison of experimental α_f spectra with corresponding calculations of the generalized optical functions. The height determined from the experimental spectra in (a) is used as the single parameter for the calculation of the theoretical optical functions in (b) which are drawn with the same vertical offsets as in (a). The qualitative features are well reproduced, a detailed functional conformity, however, cannot be expected due to the nonplanar nature of the iso-strain areas, especially for smaller values of q_r. The thick lines connect the positions of the first pronounced maxima which are the basis of the height calculation as shown in Fig. 8(b). Further noticeable matching features are the dip in intensity which develops at larger heights around the critical angle and the occurrence of a broad second maximum which moves towards lower angles for larger heights.

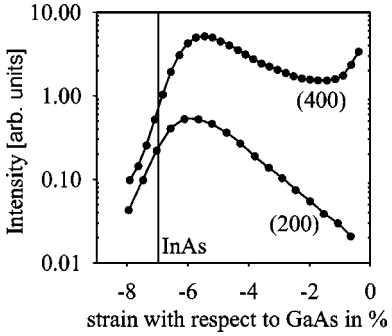

FIG. 10. Radial intensity distributions along q_r for a strong (400) and a weak (200) reflection. Instead of q_r, the corresponding strain with respect to GaAs is chosen as the axis to make both reflections comparable. The material composition of each iso-strain area is determined by the intensity ratio of both curves. The fact that the (200) intensity is getting weaker with respect to the (400) curve for smaller lattice parameter differences to the substrate shows immediately that the Ga content is larger at the bottom of the islands.

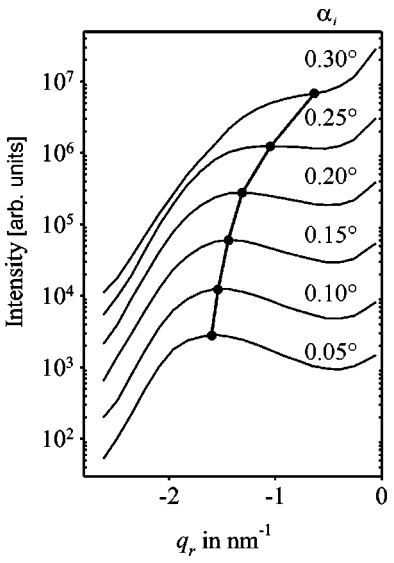

FIG. 11. Measured radial scans along q_r for various values of α_i showing an indirect influence of the generalized optical function defined in Eq. (32). Both α_i and α_f are constant for each scan. As the angle of incidence α_i is decreased, the local maxima connected by the thick line shift to smaller values of q_r. This behavior can be explained as an interaction of the optical functions of α_i and α_f.

less than 20% of the total change in half-width and has to be substracted. The remaining variation in half-width is compared to that of a hollow spherical segment with the base radius taken from the first step. The radius of curvature is then varied to achieve an optimum correspondence with the experimental data. This last step is not generalizable for arbitrary shapes but depends on the actual shape model.

Figure 9 shows the experimental α_f dependencies and the calculated generalized optical functions using Eq. (32). The optical functions are seen to dominate the low part of the α_f spectrum while the intensities for larger values of α_f can only be explained by including the vertical structure factor from Eq. (24) together with corrections for size distribution and curvature. However, the essential information—the height of the iso-strain area—is extracted from the first maximum alone, eliminating the need for complex fitting procedures.

Until recently, the picture of island formation in Stranski–Krastanov growth was restricted to the epitaxially deposited phase forming islands without interdiffusion taking place. Recent experiments,[28–31] however, suggest that this picture may be too simple and growth parameters such as temperature, flux rates, and flux ratios[32–34] are of crucial importance. Information on the chemical composition within the islands can be obtained by comparing the intensities from radial scans along q_r for a pair of strong and weak reflections,[35] such as (400) and (200) in the zinc-blende structure of InAs and GaAs. The difference of the atomic numbers of Ga and As is 2 while In has 16 more electrons than As. Since the scattering intensity for the (200) reflection in the zinc-blende structure scales as the difference of the atomic form factors, which in turn are roughly proportional to the number of electrons, the InAs (200) reflection will be about 64 times stronger than the GaAs (200) reflection. This contrast can be used to determine the concentrations of Ga and In in alloys. The measured quantity is the intensity ratio from the (400) and (200) reflections

$$p(q_r)=\left|\frac{c_{\mathrm{In}}(q_r)F^{400}_{\mathrm{InAs}}+c_{\mathrm{Ga}}(q_r)F^{400}_{\mathrm{GaAs}}}{c_{\mathrm{In}}(q_r)F^{200}_{\mathrm{InAs}}+c_{\mathrm{Ga}}(q_r)F^{200}_{\mathrm{GaAs}}}\right|^2, \tag{43}$$

where $c_{\mathrm{In}}(q_r)$ and $c_{\mathrm{Ga}}(q_r)$ are the average concentrations of In and Ga for the particular iso-strain area selected by q_r and $F^{400/200}_{\mathrm{GaAs/InAs}}$ are the structure factors of InAs an GaAs at the (400) and (200) reflections. Together with the constraint $c_{\mathrm{In}}(q_r)+c_{\mathrm{Ga}}(q_r)=1$, Eq. (43) can be resolved for $c_{\mathrm{In}}(q_r)$. The calculation is straightforward but due to the complex nature of the structure factors the final result is a long ex-

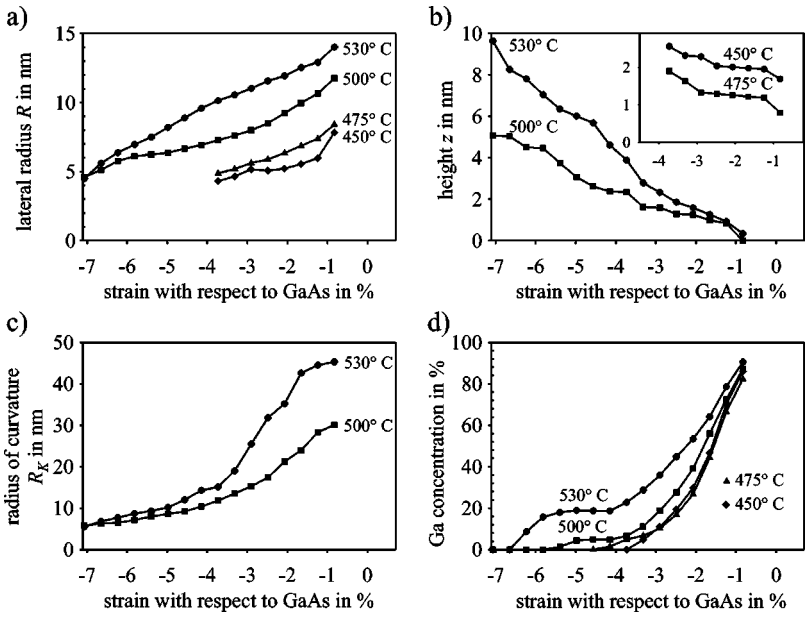

FIG. 12. Results for lateral size, height, curvature, and composition as functions of strain relative to the GaAs substrate for all four samples of the series discussed in the text. The curves for 475 °C and 450 °C are incomplete due to large relaxed clusters which prohibit any evaluation for larger strain states. Lateral size in (a) and height in (b) are seen to decrease with temperature while retaining similar functional dependencies on strain. Also, radius of curvature in (c) and Ga concentration in (d) show a monotonic decrease with decreasing temperature.

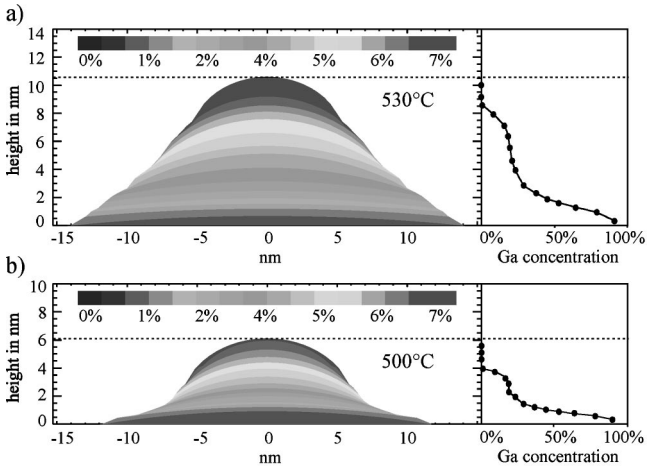

FIG. 13. Tomographic images for the samples grown at 530 °C (a) and 500 °C (b). The color coding ranges from 0% lattice parameter difference at the bottom of the islands to 7% strain with respect to GaAs at the top. The Ga concentration is displayed as a function of height on the right-hand side of each image. The dots grown at 500 °C are markedly smaller than those grown at 530 °C and show a reduced Ga concentration.

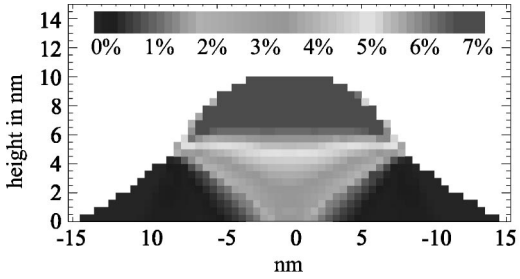

FIG. 14. Atomistic strain calculation for the sample grown at 530 °C with ''inverted cone''–In profile as suggested by recent experiments (Ref. 38). The color scale shows the strain in the [110] direction with respect to the GaAs substrate. The apparent ''resolution element'' comprises several atoms to achieve a smooth transition of colors. The laterally averaged vertical Ga concentration is the same as that of the sample grown at 530 °C. These results are in contradiction to Fig. 13.

pression and will not be reproduced here. The experimental curves are displayed in Fig. 10.

The generalized optical function derived in Eq. (32) not only influences the intensity distribution along α_f but through an indirect mechanism also that along q_r. For one fixed q_r, i.e., one particular iso-strain area, the influence of α_i and α_f factorize. The analysis of the α_f spectra as shown in Fig. 9 is therefore independent of the particular value of α_i. However, different values of q_r correspond to different heights z. Hence, the optical function varies along the radial direction. If the value of α_i is below the critical angle of the substrate α_c, there may be a certain height z and a corresponding radial position q_r where the optical function has its maximum exactly at α_i. Around that q_r, the intensity will be enhanced and may even lead to a local maximum. Such a maximum can be easily mistaken as a prevalent strain state in the strain distribution, hence care has to be taken to single out the optical effects. The maxima in Fig. 10 thus carry little useful information and a successful measurement requires extreme accuracy in the adjustment of the angles of incidence for both reflections. Figure 11 shows the dependence of the functional form of the radial scan on the value of α_i. As α_i approaches α_c, the maximum induced by the optical function of α_i vanishes entirely.

The final result of the analysis is displayed in Fig. 12 where lateral size R, height z, radius of curvature R_K, and the concentration of Ga c_{Ga} are plotted as functions of lattice parameter difference with respect to the GaAs substrate. Since all of these functions are monotonic, a unique relationship can be established between any of theses quantities. As seen in atomic force microscopy measurements (AFM), the samples grown at 475 °C and 450 °C exhibit large relaxed clumps in addition to the small coherent islands which are the principal objects of interest. Beyond a certain strain, the scattering intensity is dominated by the relaxed chunks and the contribution of the coherent islands is no longer resolvable. The maximum strains reported in Fig. 12 were chosen at discontinuities of the height functions which in both cases exhibit a small interval of negative slope beyond those values of q_r.

The fact that the heights for the samples grown at 530 °C and 500 °C saturate at a strain which corresponds to the lattice parameter of InAs, shows that the tops of these islands are covered with pure InAs. The lateral sizes decrease with decreasing temperature and are compatible with AFM pictures. As the most important result, the Ga concentration in the dots is increasing markedly with increasing growth temperature. These findings confirm and add a spatially resolved strain mapping to previous results on interdiffusion where the In content is enriched[36,28,37] or reduced,[29,38,39] depending on the composition of the epitaxially deposited material. Although the mechanism of Ga incorporation into the islands is still unclear, these measurements shed light on temperature dependence and diffusion profiles.

Finally, the information contained in the four graphs of Fig. 12 can be used to draw real space tomographic images of the islands. Figure 13 show the strain and Ga distributions for the samples grown at 530 °C and 500 °C where complete data sets are available. It has to be noted that the images do not show iso-concentration areas but iso-strain areas with their mean Ga concentration displayed on their right-hand side.

VI. ATOMISTIC CALCULATIONS OF STRAIN RELAXATION

The results presented in Sec. V quantify the strong interdiffusion of GaAs and InAs during island formation. Our method is, however, not *directly* sensitive to *lateral* variations of the In content of the dots, rather giving a laterally averaged composition. To resolve this missing link in the experimental method, we modelled strain distributions with atomistic simulations employing classical many-body interatomic potentials.[40] These potentials have been constructed to reproduce well the first-order elastic constants in GaAs and InAs.[41] Using a conjugate gradient method[42] to find the

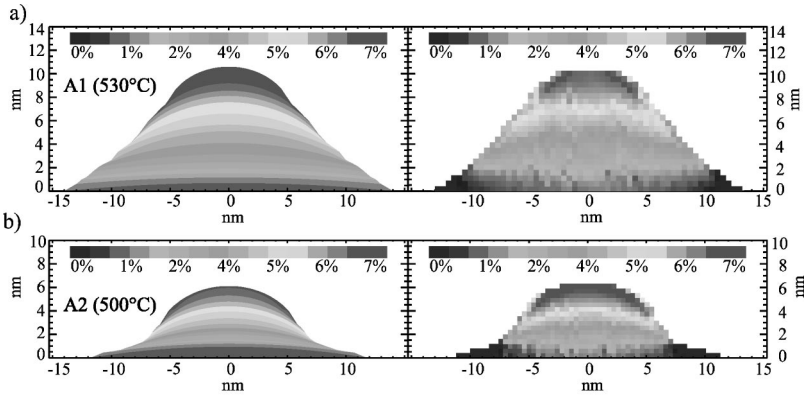

FIG. 15. Atomistic calculations of strain fields compared to experimental images. Samples grown at 530 °C (a) and 500 °C (b) have been simulated starting from an atomistic reconstruction of the islands with a lattice parameter of GaAs throughout the dot and shape and vertical Ga profile taken from Fig. 13. The lateral distribution of Ga has been assumed to be constant. Reasonable agreement is achieved for the quantitative range of strain with respect to the GaAs substrate and the curvature of the iso-strain areas which is not present in the iso-surfaces of the material composition of the atomic model. The left-hand side of both pairs of images is the experimental result, while the right-hand side shows the corresponding atomistic calculation.

closest local potential energy minimum for a set of atoms, the relaxed spatial configuration can be determined for modelled nanostructures which are initially out of equilibrium. Usually, calculations of strain fields are compared to experimental results of diffuse scattering. Since the results presented in Sec. V lead to real-space structural models, a much more direct self-consistency check between theory and experiment can be made: The experimentally determined outer shape together with the associated Ga concentration profiles for the samples grown at 500 °C and 530 °C are taken as input data for a rotationally symmetric atomistic construction of the island with all unit cells chosen to be of the size of GaAs. To be self-consistent, the strain field in the relaxed island must then match the tomographic images of the experimental evaluation.

Recent findings of Liu *et al.*[38] show that for buried $In_{0.5}Ga_{0.5}As$ quantum dots grown at 510 °C, significant lateral compositional inhomogeneity occurs, where most of the In is concentrated in an inverted cone with the tip at the bottom of the dot. If such an In distribution can be generalized to include other $In_xGa_{1-x}As$ quantum dot systems and even be explained as a property of free-standing islands, the resulting strain states should be compatible with the results of Sec. V. However, in our case of pure InAs deposition, the corresponding atomistic calculation which is shown in Fig. 14 contradicts the experimental results in Fig. 13.

Assuming a laterally homogeneous Ga profile leads to the strain distributions shown in the right-hand side of Fig. 15 where the experimentally found strain fields are compared with the outcome of the atomistic calculations for the samples grown at 530 °C and 500 °C. The good qualitative agreement between each corresponding pair of images shows that the assumption of a laterally constant composition is in accordance with the experiment.

The jagged nature of the iso-strain areas together with the appearance of surface effects in the simulated strain fields are due to the statistical nature of the dot composition. The strain relaxation simulations are carried out with one particular random configuration of In and Ga atoms having the correct depth dependence in the concentrations. In the x-ray experiments, at least 10^5 such islands—all with different configurations—contribute to the detected intensity. However, the quantitative range of strain with respect to the GaAs substrate as well as the curvature of the iso-strain areas are both reproduced in the theoretical simulation. It has to be noted that the introduction of curvature is not an artifact of the initial assumptions, since the composition in the atomistic model has planar iso-surfaces. For practical purposes, the now available information on strain and composition can thus be regarded as complete.

VII. CONCLUSION

In summary, we have established a new experimental and analytical approach for the structural analysis of semiconductor quantum dots. The scattering formalism developed in Secs. II and III allows us to qualitatively understand the intensity distribution in reciprocal space, as well as quantitatively extract geometrical information together with strain and composition profiles from the experimental data. In Sec. IV we have presented experimental concerns with respect to the appropriate scattering geometry as well as the limits of our approximations. Section V showed that experimental technique and analytical formalism can be successfully applied to a typical InAs/GaAs quantum dot system. The experimental composition profiles indicate that Ga incorporation into the islands is a heavily temperature dependent process which results in In concentrations as low as 50% for a temperature of 530 °C.

ACKNOWLEDGMENTS

We thank D. Smilgies for the excellent conditions at the TROÏKA II beamline at the European Synchrotron Radiation Facility. This work was supported by the Deutsche Forschungsgemeinschaft under Grant No. Pe 127/1-6+2 and the Academy of Finland under Project No. 45481.

[1] MRS Bull. **23**, No. 2 (1998).
[2] S. Guha, A. Madhukar, and K. C. Rajkumar, Appl. Phys. Lett. **57**, 2110 (1990).
[3] R. Leon, Science **267**, 1966 (1995).
[4] A. P. Alivisatos, Science **271**, 933 (1996).
[5] F. H. Julien and A. Alexandrou, Science **282**, 1429 (1998).
[6] D. Bimberg, M. Grundmann, and N. N. Ledentsov, *Quantum Dot Heterostructures* (Wiley, Chichester, 1999).
[7] J. M. García, G. Medeiros-Ribeiro, K. Schmidt, T. Ngo, J. L. Feng, A. Lorke, J. Kotthaus, and P. M. Petroff, Appl. Phys. Lett. **71**, 2014 (1997).
[8] Q. Shen, C. C. Umbach, B. Weselak, and J. M. Blakely, Phys. Rev. B **53**, R4237 (1996).
[9] L. De-Caro and L. Tapfer, Phys. Rev. B **49**, 11 127 (1994).
[10] V. Holỳ, A. A. Darhuber, G. Bauer, P. D. Wang, Y. P. Song, C. M. Sottomayor-Torres, and M. C. Holand, Phys. Rev. B **52**, 8348 (1995).
[11] J. L. Jordan-Sweet, P. M. Mooney, M. A. Lutz, R. M. Feenstra, J. O. Chu, and F. K. LeGoues, J. Appl. Phys. **80**, 89 (1996).
[12] Q. Shen and S. Kycia, Phys. Rev. B **55**, 15 791 (1997).
[13] G. D. U'Ren, M. S. Goorsky, E. M. Koontz, M. H. Lim, G. S. Petrich, L. A. Kolodziejski, V. V. Wong, H. I. Smith, K. M. Matney, and M. Wormington, J. Vac. Sci. Technol. B **16**, 1381 (1998).
[14] A. Ulyanenkov, N. Darowski, J. Grenzer, U. Pietsch, K. H. Wang, and A. Forchel, Phys. Rev. B **60**, 16 701 (1999).
[15] T. Baumbach, D. Lübbert, and M. Gailhanou, J. Appl. Phys. **87**, 3744 (2000).
[16] C. Giannini, T. Baumbach, D. Lübbert, R. Felici, L. Tapfer, T. Marschner, W. Stolz, N. Y. Jin-Phillipp, and F. Phillipp, Phys. Rev. B **61**, 2173 (2000).
[17] S. Di Fonzo, W. Jark, S. Lagomarsino, C. Giannini, L. De Caro, A. Cedola, and M. Müller, Nature (London) **403**, 638 (2000).
[18] A. J. Steinfort, P. M. L. O. Scholte, A. Ettema, F. Tuinstra, M. Nielsen, E. Landemark, D. M. Smilgies, R. Feidenhans'l, G. Falkenberg, L. Seehofer, and R. L. Johnson, Phys. Rev. Lett. **77**, 2009 (1996).
[19] A. A. Darhuber, P. Schittenhelm, V. Holý, J. Stangl, G. Bauer, and G. Abstreiter, Phys. Rev. B **55**, 15 652 (1997).
[20] I. Kegel, T. H. Metzger, P. Fratzl, J. Peisl, A. Lorke, J. M. García, and P. M. Petroff, Europhys. Lett. **45**, 222 (1999).
[21] M. Schmidbauer, T. Wiebach, H. Raidt, M. Hanke, R. Khler, and H. Wawra, J. Phys. D **32**, A230 (1999).
[22] Th. Wiebach, M. Schmidbauer, M. Hanke, H. Raidt, R. Köhler, and H. Wawra, Phys. Rev. B **61**, 5571 (2000).
[23] T. Wiebach, M. Schmidbauer, M. Hanke, H. Raidt, R. Köhler, and H. Wawra, Phys. Rev. B **61**, 5571 (2000).
[24] M. Rauscher, R. Paniago, H. Metzger, Z. Kovats, J. Domke, J. Peisl, H. D. Pfannes, J. Schulze, and I. Eisele, J. Appl. Phys. **86**, 6763 (1999).
[25] T. Salditt, T. H. Metzger, C. Brandt, U. Klemradt, and J. Peisl, Phys. Rev. B **51**, 5617 (1995).
[26] M. Tolan, *X-Ray Scattering from Soft-Matter Thin Films* (Springer-Verlag, Berlin, 1999), Chap. 2.
[27] P. Ehrhart, J. Nucl. Mater. **216**, 170 (1994), and references therein.
[28] N. Grandjean, J. Massies, and O. Tottereau, Phys. Rev. B **55**, R10 189 (1997).
[29] P. B. Joyce, T. J. Krzyzewski, G. R. Bell, B. A. Joyce, and T. S. Jones, Phys. Rev. B **58**, R15 981 (1998).
[30] E. Mateeva, P. Sutter, and M. G. Lagally, Appl. Phys. Lett. **74**, 567 (1999).
[31] G. Medeiros-Ribeiro, A. M. Bratkovski, T. I. Kamins, D. A. A. Ohlberg, and R. S. Williams, Science **279**, 353 (1998).
[32] A. Madhukar, Q. Xie, P. Chen, and A. Konkar, Appl. Phys. Lett. **64**, 2727 (1994).
[33] G. S. Solomon, J. A. Trezza, and J. S. Harris, Appl. Phys. Lett. **66**, 991 (1995).
[34] H. Eisele, O. Flebbe, T. Kalka, C. Preinesberger, F. Heinrichsdorff, A. Krost, D. Bimberg, and M. Dähne-Prietsch, Appl. Phys. Lett. **75**, 106 (1999).
[35] B. E. Warren, *X-Ray Diffraction* (Dover, New York, 1990), Chap. 3.3.
[36] J. Tersoff, Phys. Rev. Lett. **81**, 3183 (1998).
[37] X. Z. Liao, J. Zou, D. J. H. Cockayne, R. Leon, and C. Lobo, Phys. Rev. Lett. **82**, 5148 (1999).
[38] N. Liu, J. Tersoff, O. Baklenov, A. L. Holmes, Jr., and C. K. Shih, Phys. Rev. Lett. **84**, 334 (2000).
[39] B. Lita, R. S. Goldman, J. D. Phillips, and P. K. Bhattacharya, Appl. Phys. Lett. **75**, 2797 (1999).
[40] C. Pryor, Phys. Rev. B **57**, 7190 (1998), and references therein.
[41] K. Nordlund, J. Nord, J. Frantz, and J. Keinonen, Comput. Mater. Sci. (to be published).
[42] K. Nordlund, P. Partyka, R. S. Averback, I. K. Robinson, and P. Ehrhart (unpublished).